Sensing Behavior of Atomically Thin-Layered MoS_2 Transistors

Dattatray J. Late,[†,¶,*] Yi-Kai Huang,[†,¶] Bin Liu,[†] Jagaran Acharya,[‡,§] Sharmila N. Shirodkar,[‡] Jiajun Luo,[⊥] Aiming Yan,[†] Daniel Charles,[†] Umesh V. Waghmare,[‡] Vinayak P. Dravid,[†,*] and C. N. R. Rao[∥]

[†]Department of Materials Science and Engineering, International Institute of Nanotechnology, Northwestern University, Evanston, Illinois 60208, United States, [‡]Theoretical Science Unit, Jawaharlal Nehru Centre for Advanced Scientific Research, Jakkur PO, Bangalore 560064, India, [§]Central Department of Physics, Tribhuvan University, Kathmandu, 8212 Nepal, [⊥]Department of Electrical Engineering and Computer Science, Northwestern University, Evanston Illinois 60208, United States, and [∥]International Centre for Materials Science and CSIR Centre of Excellence in Chemistry, Jawaharlal Nehru Centre for Advanced Scientific Research, Jakkur PO, Bangalore 560064, India. [¶]These authors contributed equally to this work.

ABSTRACT Most of recent research on layered chalcogenides is understandably focused on single atomic layers. However, it is unclear if single-layer units are the most ideal structures for enhanced gas–solid interactions. To probe this issue further, we have prepared large-area MoS_2 sheets ranging from single to multiple layers on 300 nm SiO_2/Si substrates using the micromechanical exfoliation method. The thickness and layering of the sheets were identified by optical microscope, invoking recently reported specific optical color contrast, and further confirmed by AFM and Raman spectroscopy. The MoS_2 transistors with different thicknesses were assessed for gas-sensing performances with exposure to NO_2, NH_3, and humidity in different conditions such as gate bias and light irradiation. The results show that, compared to the single-layer counterpart, transistors of few MoS_2 layers exhibit excellent sensitivity, recovery, and ability to be manipulated by gate bias and green light. Further, our *ab initio* DFT calculations on single-layer and bilayer MoS_2 show that the charge transfer is the reason for the decrease in resistance in the presence of applied field.

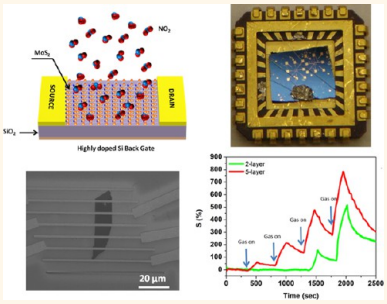

KEYWORDS: MoS_2 · gas sensor · gate bias · light irradiation · density functional theory

Graphene has attracted much attention in recent years, with many potential proof-of-concept device demonstrations, such as field effect transistors,[1−5] ultracapacitors,[6−8] solar cells,[9−12] and especially gas sensors.[13−15] For gas sensors, the prior experience of traditional semiconducting metal oxides indicates improved sensing performance with an increase in the surface-to-volume ratio.[16] This is why graphene is believed to outperform traditional sensors since one atomically thin 2-D form has exceedingly high surface-to-volume ratio. Indeed, previous reports on graphene show excellent sensing performance.[14] However, in addition to surface-to-volume ratio, other important factors for a good gas sensor include the semiconducting properties[17,18] and availability of reactive sites for redox reactions. The semiconducting behavior is particularly attractive for modulating the transport characteristics with exposure to light or gate bias to enhance sensing performance.[19,20] Graphene fails in this regard because it has zero band gap. Recently, the lack of a band gap of graphene has inspired researchers to search for other graphene-like 2-D layered semiconducting materials with appropriate band gap. To date, there are several other atomically thin-layered 2-D materials that have been identified and investigated, such as molybdenum disulfide (MoS_2),[21−33] gallium sulfide (GaS),[26,34] gallium selenide (GaSe),[26,34] hexagonal boron nitride (h-BN),[35−40] niobium diselenide ($NbSe_2$),[32,40−42] tungsten diselenide (WSe_2),[43,44] among others.

Among these emerging 2-D layered materials, MoS_2 is an n-type semiconductor and has been widely studied. More importantly, unlike graphene, the bulk MoS_2 possesses an indirect band gap (1.2 eV). Remarkably, for two-dimensional single-layer sheets, the band gap becomes direct and wider (1.8 eV). This transition from indirect band gap to direct band gap has also been confirmed by a strong photoluminescence of single-layer MoS_2.[45,46] However, in spite of excellent semiconducting properties and the possibility of large surface-to-volume ratio of atomically thin-layered MoS_2, there are few recent reports on its potential as a

* Address correspondence to datta099@gmail.com, v-dravid@northwestern.edu.

Received for review January 3, 2013 and accepted May 28, 2013.

Published online May 28, 2013
10.1021/nn400026u

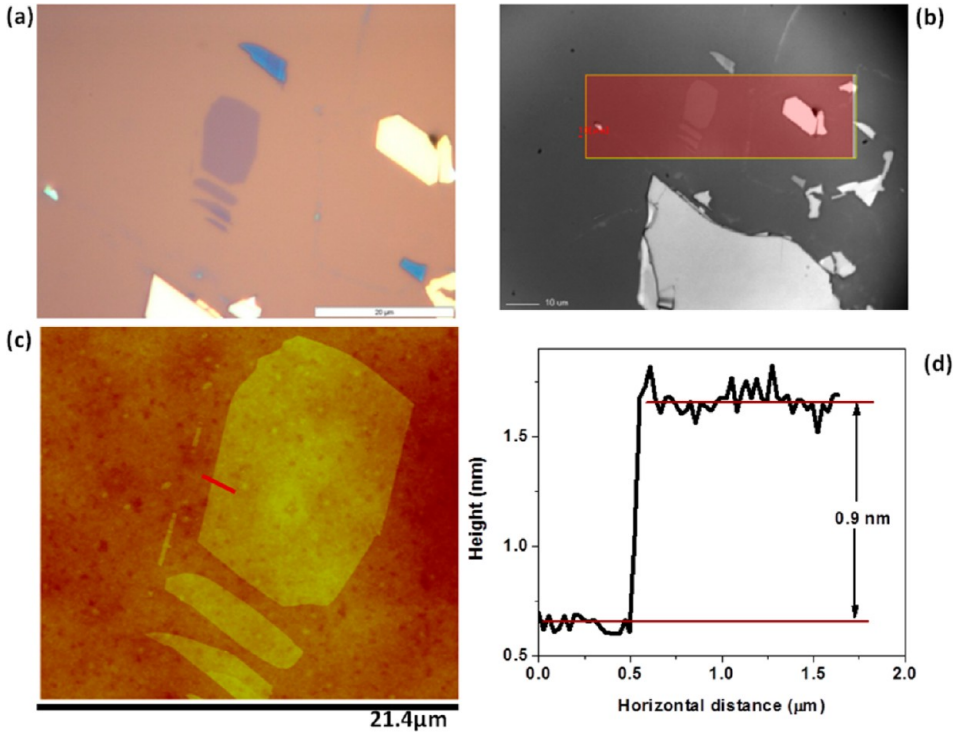

Figure 1. Single-layer MoS_2 sheet deposited on 300 nm SiO_2/Si substrate using the micromechanical cleavage method. (a) Optical image, (b) Raman image, (c) AFM image, and (d) corresponding AFM height profile.

viable and effective chemical sensor.[47−49] Further, most of these reports do not emphasize the subtleties of gas-sensing performance and its relation to layered structures but instead demonstrate gas sensing as a proof-of-concept.

Herein, for the first time, we have prepared and well-characterized single- and multiple layers of crystalline MoS_2 sheets to fabricate a transistor-based gas-sensing platform. The sensing performance of these transistors for NO_2, NH_3, and humidity with and without gate bias and light irradiation has been assessed to unravel the role of layered structures in gas−solid interactions.

RESULTS AND DISCUSSION

After the MoS_2 sheets were deposited by the mechanical exfoliation method, we used a complementary approach to confirm their thickness. Figure 1a shows an optical image of a single-layer MoS_2 sheet deposited on a 300 nm SiO_2/Si substrate using the micromechanical cleavage method. Figure 1b shows Raman image of single-layer MoS_2 sheet. Figure 1c shows the AFM image, and Figure 1d shows the corresponding quantitative AFM height profile. The measured height of a single-layer MoS_2 sheet is ∼0.9 nm (Figure 1d), which is consistent with previous reports.[26,47] For 2−5 layers of MoS_2, the measured thicknesses were approximately 1.4, 2.2, 2.5, and 3.3 nm, respectively (as shown in Supporting Information Figures S12−S15).

Figure 2 shows TEM images of few-layer MoS_2 sheets transferred onto a QuantaFoil TEM grid: Figure 2a shows the low-magnification TEM image; the inset shows the high-resolution TEM image with Mo−S spacing of 0.3−0.32 nm. Figure 2b is the high-resolution TEM image showing Moiré fringes due to the overlap of multiple MoS_2 layers; the distance between fringes is between 0.6 and 0.7 nm, which is comparable to a single layer of the S−Mo−S building block. Figure 2c shows the low-magnification TEM image of few-layer MoS_2 sheets. We have also noticed amorphization of MoS_2 layers due to high-energy electron radiation. The region is marked in a circle, as shown in Figure 2c. Figure 2d shows the selected area electron diffraction (SAED) pattern of MoS_2 layers, confirming the hexagonal structure and that the orientation of the MoS_2 sheet is along the ⟨100⟩ zone.

Raman spectroscopy gives precise and exact information about properties of the material such as fine structure, atomic bonds, thermal expansion, specific heat, thermal conductivity, crystallographic orientation, stress, chemical composition, phase transition, *etc*. Further, the localized or extended (mapping) can also be studied using micro-Raman. It is also important to know the vibrational properties of single-layer to multilayer MoS_2 sheets to understand the electron−phonon interaction and the transport properties of MoS_2 sheets, which have a large impact especially on field effect transistor device performance. Raman spectroscopy is quite sensitive to the thickness of 2-D layered material systems, and our results are consistent with the reported values.[26,50] Figure 3a shows the comparative Raman spectrum of bulk and single-layer MoS_2. Figure 3b shows the Raman spectrum of the

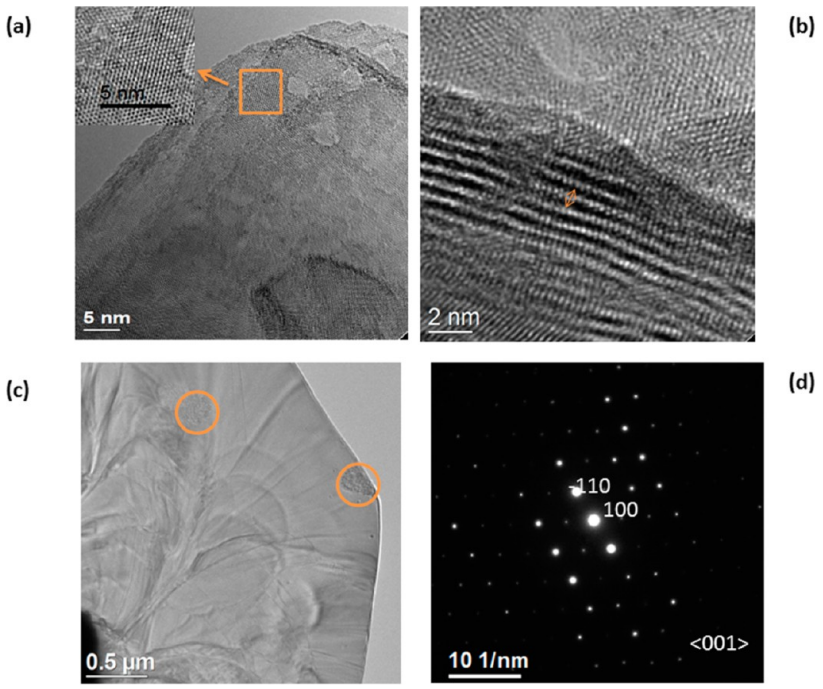

Figure 2. TEM images of few-layer MoS_2 sheets transferred onto a QuantaFoil grid. (a) Low-magnification TEM image; inset shows the high-resolution TEM image. (b) High-resolution TEM image showing Moiré fringes due to the overlap of multiple MoS_2 layers. (c) Low-magnification TEM showing electron-beam damage. (d) SAED pattern.

bilayer MoS_2 sheet before and after exposure to 1000 ppm NH_3 gas using 514 nm Ar laser irradiation. The position of E^1_{2g} and A_{1g} mode stiffens and broadens due to exposure of 1000 ppm NH_3 gas with bilayer MoS_2 sheets. Our results of the Raman spectrum on exposure to NH_3 gas is consistent with a recent report of charge transfer interaction with an electron donor molecule.[51,52] Figure 3c shows the effect of laser power variation on the peak position of the Raman E^1_{2g} mode for single-layer to six layers of MoS_2. Figure 3d shows the effect of laser power variation on FWHM of the E^1_{2g} mode for single-layer to six layers of MoS_2. Figure 3e shows the effect of laser power variation on peak position of the A_{1g} mode for single-layer to six layers of MoS_2, and Figure 3f shows the effect of laser power variation on the FWHM of the A_{1g} mode for single-layer MoS_2 to six layers of MoS_2 sheet samples. Single-layer MoS_2 to multilayer MoS_2 samples show a red shift for both E^1_{2g} and A_{1g} modes. Further, we observed the increased line width as a function of increasing laser power. The change in peak position as well as peak broadening as a function of increasing laser power indicates the increasing local temperature on the MoS_2 sheet sample surface. Thus, the Raman spectrum of MoS_2 as a function of number of layers shows laser power dependence. The E^1_{2g} and A_{1g} are sensitive to laser power variation, and change in peak position and line width of the spectra was observed.[26,53]

The gas-sensing device platform was fabricated using electron-beam lithography (E-BL) for patterning Ti/Au electrodes on top of isolated MoS_2 sheets, and back gate geometry was used. Figure 4a shows the schematic of the MoS_2 transistor-based NO_2 gas-sensing device, and Figure 4b shows the optical photograph of the sensing device mounted on the chip. The electrodes on the sample were connected to the gold pad on the chip carrier by gold wire. This chip carrier was then mounted on the stage inside the gas testing chamber for measurement. Figure 4c shows the optical image, and Figure 4d shows the SEM image of an E-beam lithography patterned two-layer MoS_2 transistor device. In a typical MoS_2 transistor device, the length of the sheet is about 30 μm, and the spacing of the electrodes is 5 μm. Extra efforts were spent during the mechanical exfoliation process to deposit large enough flakes for electrode design, which not only facilitates patterning electrodes but also helps diminish edge portion since edge sites may act differently in the gas-sensing experiment. Figure 4e shows the experimental setup used for NH_3 and NO_2 gas-sensing performance. The as-fabricated single- to five-layer MoS_2 FETs were tested with different gases at room temperature. We found that the current of the single-layer MoS_2 device was not stable over time as reported earlier,[47] while multilayer MoS_2 devices exhibited much more stable response. For clarity and brevity, we will only discuss two-layer and five-layer samples in this article because they are the thinnest and the thickest. We note that both three- and four-layer samples seem to show behavior closer to that of the five-layer sample.

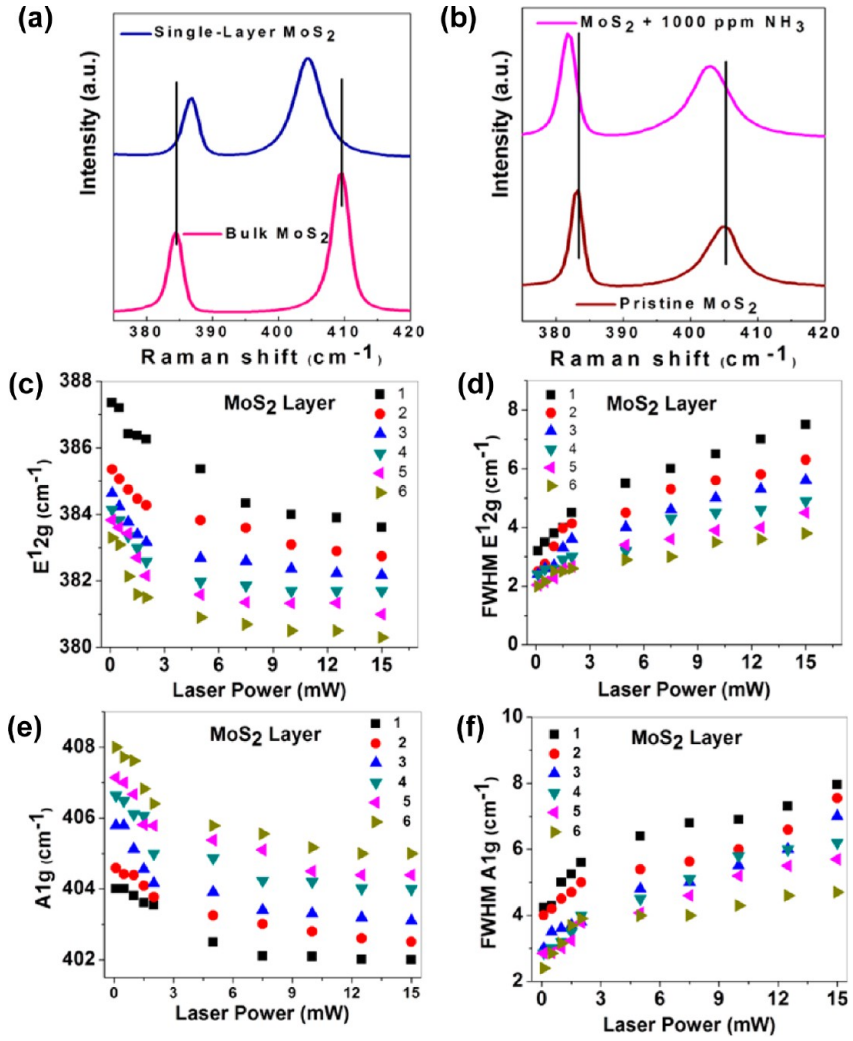

Figure 3. (a) Raman spectrum of bulk and single-layer MoS_2 sheet. (b) Raman spectrum of bilayer MoS_2 sheet before and after exposure to 1000 ppm NH_3. (c) Effect of laser power variation on peak position of the Raman E^1_{2g} mode for single-layer to six layers of MoS_2. (d) Effect of laser power variation on the FWHM of the E^1_{2g} mode for single-layer to six layers of MoS_2. (e) Effect of laser power variation on the peak position of the A_{1g} mode for single-layer to six layers of MoS_2. (f) Effect of laser power variation on the FWHM of the A_{1g} mode for single-layer to six layers of MoS_2 sheets.

Figure 5 shows the gas-sensing behavior of two-layer and five-layer MoS_2 FETs when exposed to NH_3 (Figure 5a) and NO_2 (Figure 5b). The analyte gas was injected into the chamber for 3 min, and then samples were allowed to recover for 10 min in pure nitrogen environment. There were four cycles in this experiment, and the analyte gas concentration in each cycle was chosen to be 100, 200, 500, and 1000 ppm. Sensitivity is defined as $S = (R_g - R_{N_2})/R_{N_2}$, where R_g is the resistance of the device in target gas, and R_{N_2} is the resistance of the device in dry N_2. It is well-known that NO_2 acts as an electron acceptor (p-type doping) while NH_3 acts as an electron donor (n-type doping). Thus, for n-type semiconductors, such as MoS_2, NO_2 increases its resistance while NH_3 decreases its resistance based on a charge transfer mechanism. Our results show clear response of MoS_2 layers to both NO_2 and NH_3, and the trends in resistance change confirm that the charge transfer mechanism dominates the sensing process. The recovery is often not fully complete in each cycle, which is also observed in graphene-based sensors[15] and in previous MoS_2 sensor reports.[47]

Interestingly, we notice that the five-layer MoS_2 sample has better sensitivity compared to that of the two-layer MoS_2 sample, which seems counterintuitive. We should point out that samples were tested multiple times with more than 1 day interval between the tests to allow full recovery of test samples, but the results remained the same. This phenomenon may be due to the different electronic structures when thicknesses (layering) are dissimilar. The energy levels of conduction and valence band of MoS_2 changes with size, as shown in an earlier report,[54] and thus they may likely alter the redox potentials, which in turn affect the sensing ability of MoS_2. Clearly, this is a complex issue and still under study to clarify the specific sensing mechanism.

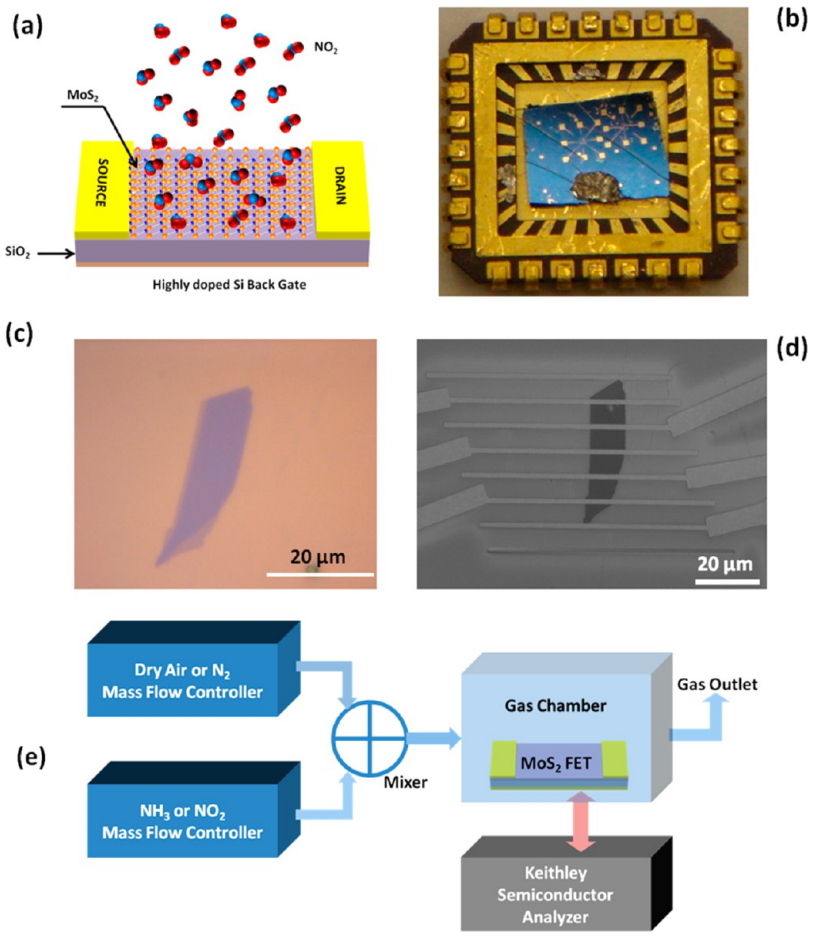

Figure 4. (a) Schematic of the MoS_2 transistor-based NO_2 gas-sensing device. (b) Optical photograph of the MoS_2 sensing device mounted on the chip. (c) Optical image of two-layer MoS_2 sheet. (d) SEM image of two-layer MoS_2 transistor device, and (e) experimental setup used for NH_3 and NO_2 gas-sensing performance.

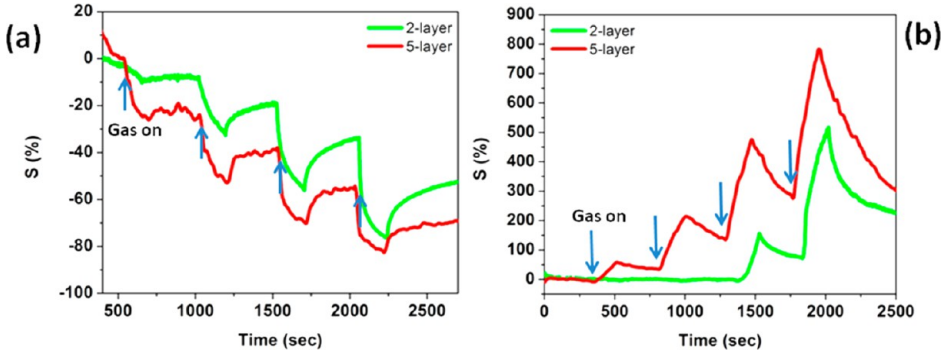

Figure 5. Comparative two- and five-layer MoS_2 cyclic sensing performances with (a) NH_3 and (b) NO_2 (for 100, 200, 500, 1000 ppm).

In addition to the cyclic experiments shown in Figure 5, we also have carried out measurements of I_{ds} (drain-source current)$-V_{gs}$ (gate-source voltage) curves with fixed V_{ds} (drain-source voltage) before and after exposure to NH_3 and NO_2, as shown in Supporting Information Figure S3. This shows that the semiconducting property of MoS_2 sheets can be tuned by exposure to gases. Figure 6 shows the comparative sensing behavior with and without applying back gate voltage (+15 V) for two-layer NH_3 (Figure 6a) and NO_2 (Figure 6b) and five-layer MoS_2 NH_3 (Figure 6c) and NO_2 (Figure 6d). As mentioned in the introduction, resistance in MoS_2 can be tuned by gate biasing, which makes MoS_2 more competitive for gas sensing compared to graphene-based sensors. Interestingly, applying back gate voltage affects gas-sensing responses differently for reducing gas (NH_3) and oxidizing gas (NO_2). Applying positive back gate voltage enhances sensitivity for NO_2, while decreasing sensitivity for NH_3. The phenomena can be understood

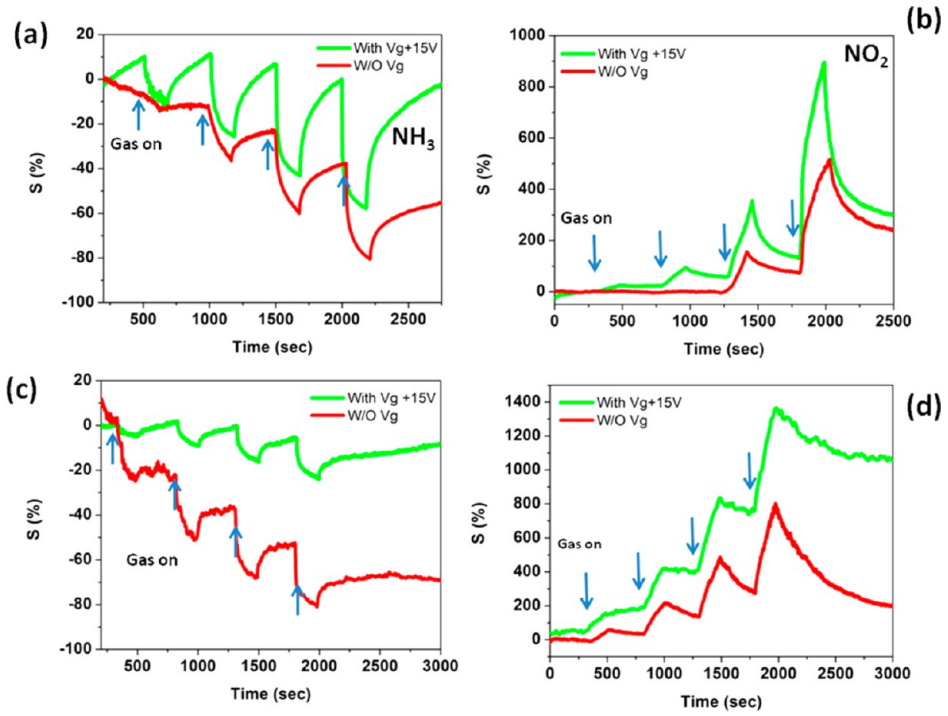

Figure 6. Comparative sensing behavior with and without applying back gate voltage (+15 V) for two-layer (a) NH_3, (b) NO_2 and five-layer MoS_2 (c) NH_3 and (d) NO_2 (for 100, 200, 500, 1000 ppm).

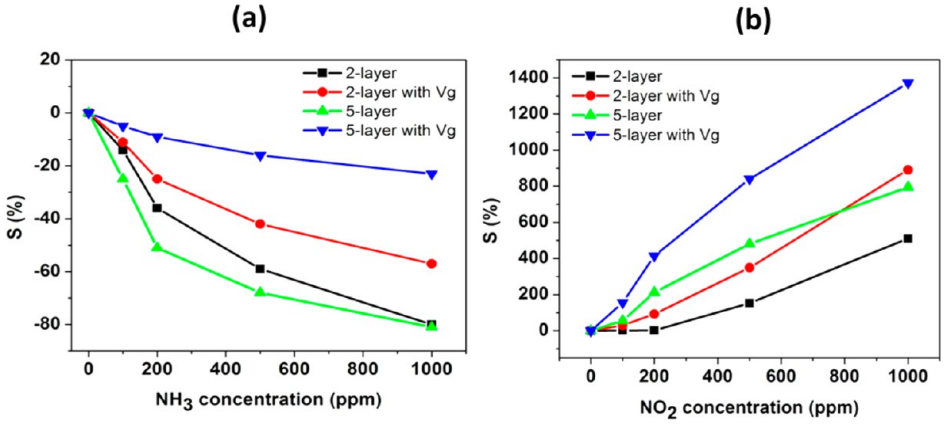

Figure 7. Sensitivity as a function of concentration (in ppm) for two-layer and five-layer MoS_2 sheets for (a) NH_3 and (b) NO_2.

as follows: when positive gate voltage is applied, electrons accumulate at the interface of MoS_2 and SiO_2, so for NO_2, which is an electron acceptor, it has more electrons to accept. However, for NH_3, which is an electron donor, the electric field built up at the interface repels NH_3 to donate an electron, which in turn decreases the gas sensitivity. Furthermore, by comparing the change in sensitivity with and without gate bias, the five-layer MoS_2 sample showed stronger response to gate bias, which suggests that carrier concentration in five-layer MoS_2 is more susceptible to the influence of gate bias. This can be further confirmed by the higher ON/OFF ratio of the five-layer sample shown in Supporting Information Figure S3. The ON/OFF ratio of five-layer MoS_2 is 5.5×10^5, compared to 7.5×10^2 of two-layer MoS_2. This gate-dependent selectivity can be effectively utilized to make MoS_2 sensors more selective to certain type of gases, as this is a much easier approach than incorporating dopants into material which is the common way to make sensors selective to certain test gas.[55] Figure 7 shows the summary of sensitivity as a function of concentration (in parts per million) for two-layer and five-layer MoS_2 sensor devices in different operational situations with exposure to (a) NH_3 and (b) NO_2. The highest sensitivity toward NO_2 was achieved on the five-layer MoS_2 sample operated with positive gate voltage. The highest sensitivity toward NH_3 was achieved on the five-layer MoS_2 sample operated without gate voltage. Their sensitivities when exposed to

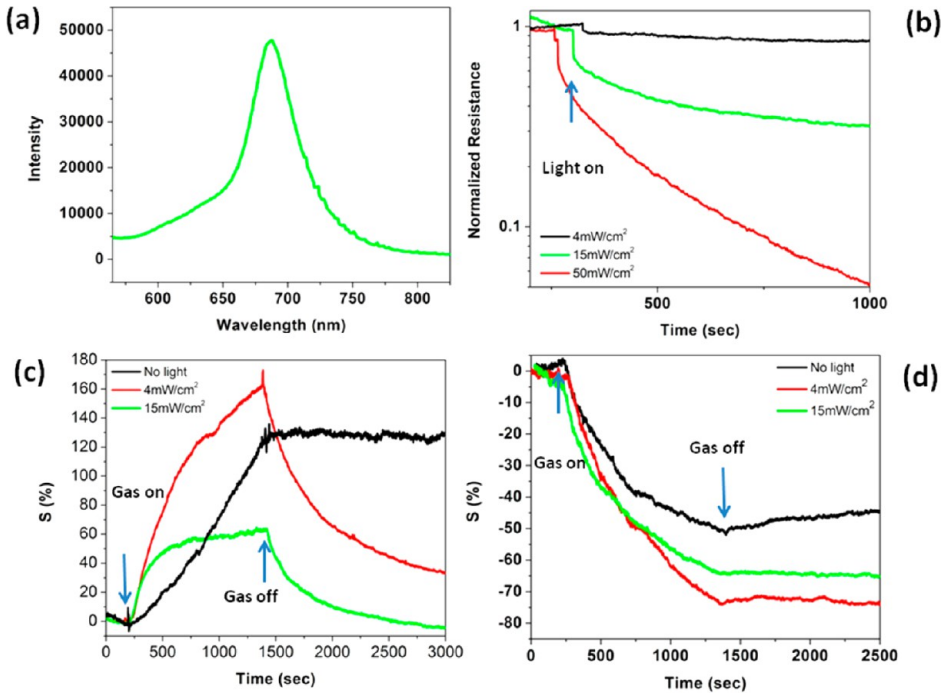

Figure 8. (a) Photoluminescence spectra of five-layer MoS_2. (b) Change of normalized resistance under light irradiation. (c) Sensing behavior of five-layer MoS_2 exposed to 100 ppm NO_2 under green light illumination. (d) Sensing behavior of five-layer MoS_2 exposed to 100 ppm NH_3 under green light illumination.

1000 ppm NO_2 and NH_3 were determined to be 1372 and 86%, respectively.

Other than applying gate bias, light exposure is long believed to help increase sensitivity and shorten recovery time[19] attributed to varied mechanisms. We applied the same approach to the five-layer MoS_2 sample for a series of light-assisted sensing experiments. Figure 8a shows the photoluminescence (PL) spectrum of the five-layer MoS_2 sample with a peak located at 687 nm, confirming the existence of finite band gap in the material, and the result is similar to the reported value.[45,46] To further examine the influence of light irradiation, we then exposed the sample to green LED (532 nm) whose power density can be tuned by changing currents running through it and recorded the variation of resistance. From Figure 8b, it can be seen that resistance goes down when the sample is irradiated by light, and the magnitude depends on the illuminated power density (the three curves are deliberately shifted horizontally for clarity).

The influence of light can be divided into two stages: at first stage, resistance drops quickly with a small amount, and at second stage, resistance slowly reaches saturation with a larger amount. From a recently published report,[56] the photocurrent generated in monolayer MoS_2 is attributed mostly to heat rather than exciton, which explains in our MoS_2 sensor device that the second stage of photocurrent is more dominant than the first stage, especially that five-layer MoS_2 is an indirect semiconductor while monolayer MoS_2 is a direct semiconductor. Figure 8c,d shows the gas-sensing behavior of the five-layer MoS_2 sample reacting with NO_2 and NH_3, respectively, under green light irradiation with different power densities. Although many similar light-assisted sensing experiments use UV light as the source, the damage of UV light needs to be taken into account, as shown in a report of carbon-based sensors.[57] Furthermore, since the device showed response to green light, we decided to use it to minimize damage. Further, the SEM and optical microscope were used to observe the effect of green light irradiation, which showed no obvious and apparent damage caused after long-time green light exposure. In order to compare the response and recovery, we injected analyte gas for a longer time (20 min) and also let the device recover for a longer time (30 min). For NO_2, the sensitivity increased when exposed to 4 mW/cm^2 irradiation but decreased when exposed to 15 mW/cm^2. It is similar to the behavior of UV-assisted metal oxide sensors, for which the power density of light has an optimal value.[58] There are two possible reasons; one is that when the power density is too high, not all the excited electrons/holes get to react with gas molecules, so the portion of reacted carriers decreases; and the other possible reason is that the desorption rate increases more than the adsorption rate because of the light-induced activation under irradiation. For response and recovery, it is obvious that the higher the power density, the quicker the response/recovery. However, in the case of NH_3, as shown in Figure 8d, the behavior is different. Although the sensitivity still has an optimal value, where

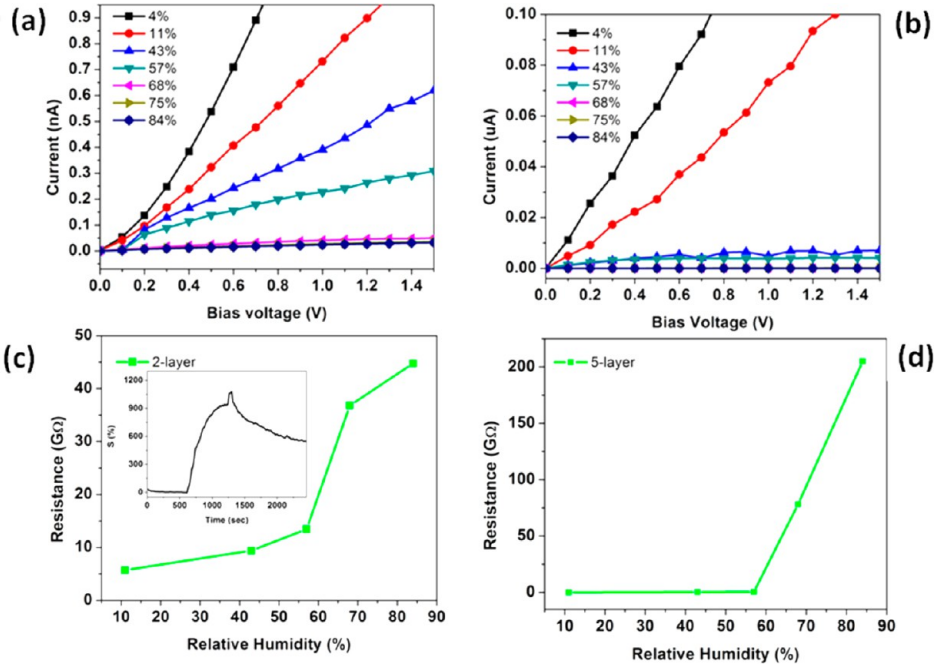

Figure 9. Current−voltage (*I*−*V*) behaviors measured under different RH values, showing an obvious slope decreasing with the increasing of RH for (a) two-layer and (b) five-layer MoS_2 sample. RH as a function of resistance for (c) two-layer and (d) five-layer MoS_2 samples. Inset of (c) shows response and recovery for change in RH from dry air (4%) to 84% RH. Response time is quick, but recovery is longer for MoS_2 layered material samples.

4 mW/cm^2 gave the highest sensitivity, the response and recovery did not show a difference whether the sample was exposed to light or not. Higher power density was also tried as shown in Supporting Information Figure S4, which indicated the response/recovery behavior still does not change. To confirm whether NH_3 is the special case, we have also performed similar experiment on H_2S, as shown in Supporting Information Figure S5, and there is no clear difference from NH_3. It implies that the kinetic energy barrier for reducing gas molecules to leave the MoS_2 surface is likely higher than that of NO_2. To our knowledge, this is the first report that light irradiation does not appreciably assist in response/recovery, and further studies are warranted to shed further light on this observation.

The humidity sensing performance of two-layer and five-layer MoS_2 sensor devices was also investigated to complete the sensing portfolio. A recent study concluded that a single-layer MoS_2 device does not respond to water vapor.[49] However, another previous work[54] showed that nano-MoS_2 reacted with water, and our own prior results also showed that the current−voltage (*I*−*V*) behavior of MoS_2 changed in the presence of water vapor.[30,31] In this work, we measured the *I*−*V* behavior under different relative humidity (RH) values, and results showed obvious decrease in the slope of *I*−*V* curves with an increase in RH, as shown in Figure 9a for the two-layer MoS_2 sensor device and Figure 9b for the five-layer MoS_2 sensor device. Water vapor is considered to be an electron acceptor just like NO_2, so the resistance of MoS_2 increases with the RH value. Once again, this observation further confirms that charge transfer mechanism is dominant in this process. Figure 9c,d shows the resistances as functions of RH of two-layer MoS_2 and five-layer MoS_2 sensor devices, respectively. The inset of Figure 9c shows response and recovery for change in RH from dry air (4%) to 84% RH.

To understand the experimental results on the sensing behavior of thin-layered MoS_2 transistors, we have carried out the *ab initio* calculations on single- and bilayer MoS_2. A 3 × 3 supercell of MoS_2 was constructed to study the adsorption of NO_2 and NH_3 on both single-layer (ABA stacking of intralayer S−Mo−S atoms) and bilayer (ABA, BAB stacking sequence of the adjacent layers) MoS_2.[59] We have computed energy of adsorption for both NH_3 and NO_2 gases on mono- and bilayer MoS_2 using the following expression

$$E_{ads}[MoS_2 + X] = E_T[MoS_2 + X] - E_T[MoS_2] - E_T[X]$$

where $E_T[MoS_2 + X]$ is the total energy of the supercell and molecule, $E_T[MoS_2]$ is the total energy of the MoS_2 slab, and $E_T[X]$ is the energy of the adsorbed molecule. The adsorption energy for both NH_3 and NO_2 on single- and bilayer MoS_2 was estimated in the presence and absence of external electric field of 0.0001 au (which is equivalent to V_g = 15 V). Our results show that there is a very slight increase in the adsorption with an increase in the number of MoS_2 layers (*i.e.*, from single-layer to bilayer), hence indicating very small increase in sensitivity for five layers as compared to two layers. The adsorption energy of NO_2 is greater than that of NH_3

TABLE 1. Comparison of Adsorption Energy for Different Supercell Configurations (kJ/mol)

supercell	V_g = 0 V	
gas	NH_3	NO_2
single-layer MoS_2	−14.44	−24.94
bilayer MoS_2	−15.75	−27.56

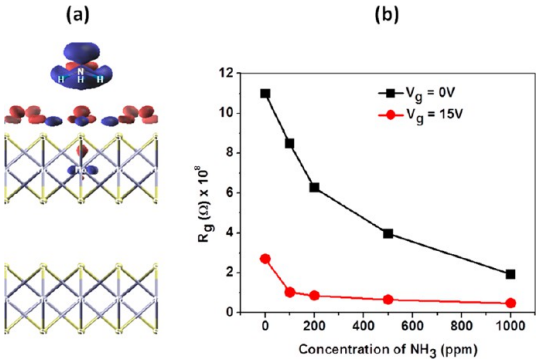

Figure 10. (a) Charge transfer in NH_3 on bilayer MoS_2 with V_g = 0 V. The red isosurface indicates negative charge, and blue isosurface denotes positive charge. (b) Variation of resistance for NH_3 on bilayer MoS_2 with V_g = 0 and 15 V.

TABLE 2. Comparison of Charge Transfer for Different Configurations (Electrons/Cell)[a]

supercell	V_g = 0 V		V_g = 15 V	
gas	NH_3	NO_2	NH_3	NO_2
bilayer MoS_2	−0.009	+0.097	−0.018	+0.089

[a] Negative is for charge transferred to MoS_2, and positive is for charge transferred from MoS_2.

for both single-layer and bilayer MoS_2, as shown in Table 1. The higher the adsorption energy, the higher its binding with the substrate, and hence MoS_2 is more sensitive to NO_2 than NH_3.

We have also estimated the amount of charge transferred between MoS_2 and NH_3, NO_2 gases in the presence and in the absence of external electric field. MoS_2 is an n-type semiconductor, implying an excess of electrons and hence conducting. NH_3 acts as an electron donor and donates electrons when absorbed on MoS_2, as shown in Figure 10a. In the presence of a positive gate voltage, electrons in the NH_3 molecule are attracted to the MoS_2, which leads to more electrons transferred to MoS_2 as compared to the number of electrons transferred in the absence of an electric field, as shown in Table 2. Due to the increase in charge carrier resistance, the MoS_2 sheet decreases and is in agreement with experimental observations, as shown in Figure 10b. With the increase in the concentration of NH_3, the charge transferred to the MoS_2 sheet increases. Due to the increase in repulsive energy between the transferred electrons and incipient electrons in MoS_2, further transfer of electrons slows with

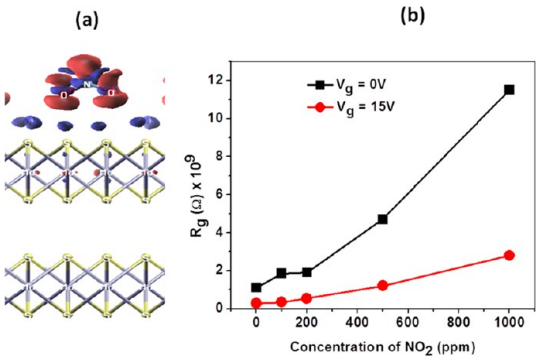

Figure 11. (a) Charge transfer in NO_2 on bilayer MoS_2 with V_g = 0 V. The red isosurface indicates negative charge, and blue isosurface denotes positive charge. (b) Variation of resistance for NO_2 on bilayer MoS_2 with V_g = 0 and 15 V.

concentration of gas. Hence, the resistance of the MoS_2 sheet decreases at first significantly and decreases slowly after a certain concentration, as shown in Figure 10b.

On the other hand, NO_2 acts as an electron acceptor and accepts electrons from the MoS_2 sheet, as shown in Figure 11a. This charge transfer reduces the number of electrons in the MoS_2 sheet, thus reducing the charge carriers in it. On application of a positive gate voltage, the electrons in the MoS_2 sheet are attracted toward the gate, thus reducing the charge transferred to NO_2, as shown in Table 2. Hence, the resistance of the substrate decreases with the application of external field. With the increase in the concentration of NO_2, more charges are transferred from MoS_2 to NO_2. The charges are transferred to different NO_2 molecules as the concentration increases, and unlike NH_3, there is no repulsion between these charges. Hence, resistance of the MoS_2 sheet steeply increases with the concentration of NO_2, as shown in Figure 11b. Our first-principles calculations are hence in agreement with experimental observations.

Our calculations explain the changes in overall resistance of the MoS_2 channel with gas adsorption and gate voltage. However, to understand the trends in the relative resistance with gate voltage, we find that the resistance of the contact of MoS_2 with Ti/Au electrodes is also relevant in addition to the charge transfer mechanism. The variation of electrostatic potential of the bulk MoS_2 along the z direction (along the direction perpendicular to the MoS_2 planes) with and without electron doping shows a high barrier of ≈11.56 eV between the MoS_2 layers, as shown in Figure 12. This implies that the electrons have to cross over a large barrier for movement toward the gate and that electrons mostly from the topmost single-layer and its contact with source and drain electrodes determine the electrical properties of the transistor. In the presence of positive gate voltage, the electrons of the Ti/Au electrode accumulate at the MoS_2 and Ti/Au contacts at the source and drain, reducing the

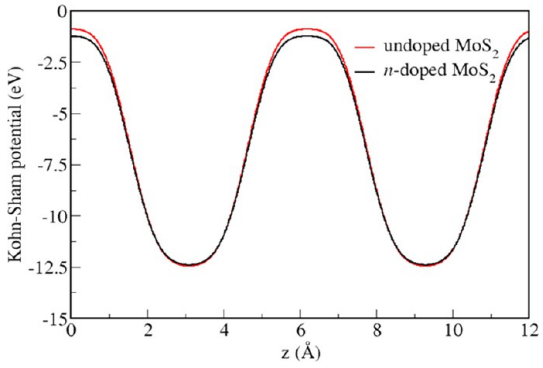

Figure 12. Variation of macroscopic average of the Kohn–Sham potential for bulk MoS_2 with and without electron doping along the *z* direction.

barrier between the Ti/Au electrodes and the MoS_2 sheet and easing the transfer of electrons across the contacts. Hence, even in presence of the ambient N_2 gas (zero concentration of NH_3 or NO_2), a large reduction in the resistance is observed with the application of gate voltage, which is responsible for the observed trends in the relative changes in the channel resistance.

CONCLUSION

We report a comprehensive suite of sensing behavior of MoS_2 atomically thin-layered structures in a transistor geometry. Isolated MoS_2 sheets were prepared on 300 nm SiO_2/Si substrates using micromechanical exfoliation and characterized for their thickness and layering with an optical microscopy, AFM, and Raman spectroscopy. Surprisingly, compared to the bilayer MoS_2 device, multilayer MoS_2 FETs showed more sensitive response to NH_3, NO_2, and also water vapor at room temperature and atmospheric pressure. We also successfully manipulated sensing behavior of MoS_2 by applying either gate bias or light exposure, which provide opportunities to improve sensing behavior and make MoS_2 to selectively respond to certain kinds of gases. Although the exact sensing mechanism of MoS_2 behavior is unclear and clearly has subtleties and nuances, it shows excellent sensing properties, worthy of further investigation. Our first-principles calculation shows that the charge transfer between the molecule and MoS_2 sheet channel is responsible for the decrease in resistance with applied field and suggests that the effect of contact resistance is also relevant to the observed changes in relative resistance. The contact resistance between the electrodes and MoS_2 layers is also an important underlying factor for the decrease in sheet resistance in the absence of absorbed gas (in the presence of N_2).

EXPERIMENTAL METHODS

Marker on SiO_2/Si Substrate. For making markers, thermal evaporation was used to deposit Cr/Au (1 nm/50 nm) on a 300 nm SiO_2/Si wafer with 200 μm × 200 μm squares with a separation of 1.5 mm (as shown in Supporting Information Figures S34 and S35) using shadow mask purchased from Photo Etch Technology, Lowell, MA (USA). Then substrates were cut into 10 mm × 10 mm square pieces using a diamond cutter pen purchased from SPI (USA) followed by standard substrate cleaning.

SiO_2/Si Substrate Cleaning. First, SiO_2/Si substrates were thoroughly cleaned by boiling substrates in acetone for 5 min and then boiling in IPA for 5 min followed by drying using dry N_2 gas. Finally, substrates were cleaned using O_2 plasma cleaning for 1 min.

Preparation of MoS_2 Sheets Using the Micromechanical Exfoliation Method. Bulk MoS_2 crystal (purchased from SPI Supplies Inc., USA, crystal size small, #429MM-AB 15 mm × 9 mm). MoS_2 crystals were collected by a professional geologist at Otter Lake deposit in Ontario, Canada. Single-layer to few-layer MoS_2 sheets were deposited at room temperature in ambient conditions by mechanically exfoliating the bulk MoS_2 crystal onto precleaned 300 nm SiO_2/Si. First, the Scotch-tape was put on the MoS_2 bulk crystals, and then we repeatedly peeled off MoS_2 to find thin flakes. The next step was to transfer these thin MoS_2 flakes onto the SiO_2/Si substrate by pressing the tape onto the substrates. Special care has been taken to exfoliate large-area MoS_2 sheets. First, the Scotch-tape was lightly pressed onto the MoS_2 bulk crystal and then removed carefully with a small angle as possible. Then peeling of the MoS_2 with Scotch-tape was done. We repeatedly peeled the MoS_2 on Scotch tape as long as we observed the light green color of MoS_2 flakes on the Scotch tape. The next step we followed was to transfer this light green color of MoS_2 flakes on Scotch tape onto the SiO_2/Si substrate. We used plastic tweezers to put pressure on the Scotch tape horizontally from one side to the other side of the SiO_2 substrate for 30–60 s. This technique gives individual tens of micrometers to 50 × 50 μm single-layer and few-layer MoS_2 sheets. Contaminants from the Scotch tape were removed by dipping the substrates in acetone for 5 min.

Optical Microscopy. The optical microscopic images were acquired with an optical microscope (Nikon Eclipse ME600) imager M1m with white light illumination (100 W halogen lamp, HAL100) using bright-field imaging modes and 100× objectives as described earlier.[26]

Atomic Force Microscopy. AFM tapping mode images were recorded using an ICON system (Bruker, Santa Barbara, CA, USA).

Raman Spectroscopy and Raman Imaging. Raman spectra and Raman imaging were done in back scattering geometry using the Nanophoton Raman-11 system with a 532 nm line of an Ar ion laser with laser power ~1 mW as described earlier.[26]

Raman Spectroscopy in NH_3 Gas. Raman spectra of MoS_2 in the presence of NH_3 has been observed to prove n-type doping in a glass chamber (as shown in Supporting Information Figure S33) that consists of a gas inlet and outlet. To avoid the effect of ambient oxygen, which can cause the Raman shift in vibration modes by attacking the Mo–S–Mo bands, initially Ar gas was passed in test chamber to stabilize the MoS_2 sample for 30 min. Then 1000 ppm NH_3 gas was passed in the test chamber. Raman spectra were recorded before and after the test gas was injected in the chamber.

MoS_2 FET-Based Gas Sensor Device Fabrication. MoS_2 FET devices were fabricated using electron-beam lithography as described earlier.[30,31,34] Electrodes were patterned by electron-beam lithography (EBL) followed by thermal evaporation to deposit titanium/gold (3 nm/70 nm). After metal deposition, samples were annealed in Ar atmosphere at 200 °C for 2 h to improve contact. For the back gate electrode, we simply scratched the surface and put indium metal as the contact. Samples were then wire bonded to the chip by gold wire to connect to the gas-sensing setup.

NO_2 and NH_3 Gas Sensor Test. Gas-sensing experiments were carried out in a home-built gas-sensing experimental setup,

as shown in Figure 4e. Gases we used for the test were NO_2 (2% NO_2 with 98% N_2) and NH_3 (1% NH_3 balances 99% N_2) cylinders purchased from Airgas Company (Port Allen, LA, USA). They were then mixed with pure nitrogen to achieve desirable concentrations before being injected into chamber. Mass flow controllers were used to control the concentration, and the total flow rate was 1000 sccm for the whole time. The testing chamber was a 250 mL flask, and gas should fill the chamber within 30 s based on the flow rate we used. The gas inlet was designed to point directly onto the sample with a distance of ~5 mm. Such a setup is for quick response to the change in environment. All the gas-sensing experiments were carried out at room temperature and at room atmospheric pressure.

Green Light Illumination. Green light illumination was carried out by using a LED head purchased from Sunlite Company (Lawrence, KS, USA). It was connected to a Keithley 2420 semiconductor to provide power, and the power density can be tuned by changing the current running through it. Electrical characterization and resistance change during gas injection were recorded with a Keithley 4200 semiconductor characterization system.

Humidity Sensor Test. For the humidity test, humidity was obtained using saturated salt solutions of various salts as described earlier by us for the graphene sensor.[13]

Electrical Characterization. Electrical characterization of field effect transistor-based sensing devices was performed by using a Keithley 4200 semiconductor characterization system to record the I_{ds} (drain-source current) change in real time (data acquisition time ~1 s) using the two-probe in a glass chamber. During the gas-sensing test, the MoS_2 sensor devices were always stabilized in nitrogen before testing, which usually took 30 min. All gate-bias-assisted and light-assisted tests were done on the same MoS_2 device to eliminate inaccuracy from device difference. Between each test, the MoS_2 sensor device was stored in a vacuum box to speed recovery, and we made sure the MoS_2 sensor device was fully recovered by checking that starting resistances were identical.

Computational Details. Our first-principles calculations are based on density functional theory (DFT) with a generalized gradient approximated (GGA) exchange correlation energy functional of Perdew–Burke–Ernzerhof (PBE)[60] as implemented in the Quantum Espresso code.[61] Ultrasoft pseudopotentials[62] were used to capture the interaction between ionic cores and valence electrons. We use an energy cutoff of 30 Ry for the plane-wave basis used for the wave functions and 180 Ry to represent the charge density. We have included semiempirical dispersive van der Waals (vdW) interaction using Grimme parametrization.[63] A $3 \times 3 \times 1$ supercell was used to simulate the adsorption of NH_3 and NO_2 molecules with 1 molecule per supercell. Due to periodic boundary conditions, this geometry corresponds to 6.27×10^{13} molecules/cm^2. Integrations over the Brillouin zone were carried out using a regular mesh of $3 \times 3 \times 1$ k-points (for the structural relaxation) of the supercell and at the zone center for a single molecule. We have increased a denser mesh of $6 \times 6 \times 1$ k-points for the charge transfer calculation. The amplitude of applied electric field was 0.0001 au, which corresponds to the back gate voltage (V_g) of +15 V applied in the experiments. The system was structurally relaxed until the maximum Hellmann–Feynmann force acting on each atom was less than 0.001 Ry/Å (for both, with and without electric field).

Conflict of Interest: The authors declare no competing financial interest.

Acknowledgment. D.J.L. would like to thank Indo-US Science & Technology Forum (IUSSTF) for a postdoctoral fellowship. The research was primarily supported by an Indo-US Science & Technology Forum (IUSSTF) grant between JNCASR, India, and Northwestern University, USA. Partial support by NSF-MRSEC and NSF-NSEC programs at NU is gratefully acknowledged. The research made use of NU*ANCE* Center and BIF facilities and Micro Fabrication Facility supported by the MRSEC program of the National Science Foundation (DMR-1121262) at the Materials Research Center of Northwestern University.

Supporting Information Available: AFM, SEM, optical microscopy and Raman spectroscopy, and Raman mapping of single-layer and multilayer MoS_2 sheets. Single- and few-layer MoS_2 based transistor device characteristics. This material is available free of charge *via* the Internet at http://pubs.acs.org.

REFERENCES AND NOTES

1. Novoselov, K. S.; Jiang, D.; Schedin, F.; Booth, T. J.; Khotkevich, V. V.; Morozov, S. V.; Geim, A. K. Two-Dimensional Atomic Crystals. *Proc. Natl. Acad. Sci. U.S.A.* **2005**, *102*, 10451–10453.
2. Novoselov, K. S.; Geim, A. K.; Morozov, S. V.; Jiang, D.; Zhang, Y.; Dubonos, S. V.; Grigorieva, I. V.; Firsov, A. A. Electric Field Effect in Atomically Thin Carbon Films. *Science* **2004**, *306*, 666–669.
3. Novoselov, K. S.; Geim, A. K.; Morozov, S. V.; Jiang, D.; Katsnelson, M. I.; Grigorieva, I. V.; Dubonos, S. V.; Firsov, A. A. Two-Dimensional Gas of Massless Dirac Fermions in Graphene. *Nature* **2005**, *438*, 197–200.
4. Schwierz, F. Graphene Transistors. *Nat. Nanotechnol.* **2010**, *5*, 487–496.
5. Liao, L.; Bai, J.; Cheng, R.; Lin, Y.; Jiang, S.; Qu, Y.; Huang, Y.; Duan, X. F. Sub-100 nm Channel Length Graphene Transistors. *Nano Lett.* **2010**, *10*, 3952–3956.
6. Wang, Y.; Shi, Z. Q.; Huang, Y.; Ma, Y. F.; Wang, C. Y.; Chen, M. M.; Chen, Y. S. Supercapacitor Devices Based on Graphene Materials. *J. Phys. Chem. C* **2009**, *113*, 13103–13107.
7. Vivekchand, S. R. C.; Rout, C. S.; Subrahmanyam, K. S.; Govindaraj, A.; Rao, C. N. R. Graphene-Based Electrochemical Supercapacitors. *J. Chem. Sci.* **2008**, *120*, 9–13.
8. Stoller, M. D.; Park, S.; Zhu, Y.; An, J.; Ruoff, R. S. Graphene-Based Ultracapacitors. *Nano Lett.* **2008**, *8*, 3498–3502.
9. Arco, L. G.; Zhang, Y.; Schlenker, C. W.; Ryu, K.; Thompson, M. E.; Zhou, C. Continuous, Highly Flexible and Transparent Graphene Films by Chemical Vapor Deposition for Organic Photovoltaics. *ACS Nano* **2010**, *4*, 2865–2873.
10. Yang, N.; Zhai, J.; Wang, D.; Chen, Y.; Jiang, L. Two-Dimensional Graphene Bridges Enhanced Photoinduced Charge Transport in Dye-Sensitized Solar Cells. *ACS Nano* **2010**, *4*, 887–894.
11. Jang, Y. H.; Xin, X.; Byun, M.; Jang, Y. J.; Lin, Z.; Kim, D. H. An Unconventional Route to High-Efficiency Dye-Sensitized Solar Cells *via* Embedding Graphitic Thin Films into TiO_2 Nanoparticle Photoanode. *Nano Lett.* **2012**, *12*, 479–485.
12. Li, X.; Zhu, H.; Wang, K.; Cao, A.; Wei, J.; Li, C.; Jia, Y.; Li, Z.; Li, X.; Wu, D. Graphene-on-Silicon Schottky Junction Solar Cells. *Adv. Mater.* **2010**, *22*, 2743–2748.
13. Ghosh, A.; Late, D. J.; Panchakarla, L. S.; Govindaraj, A.; Rao, C. N. R. NO_2 and Humidity Sensing Characteristics of Few-Layer Graphene. *J. Exp. Nanosci.* **2009**, *4*, 313–322.
14. Schedin, F.; Geim, A. K.; Morozov, S. V.; Hill, E. W.; Blake, P.; Katsnelson, M. I.; Novoselov, K. S. Detection of Individual Gas Molecules Adsorbed on Graphene. *Nat. Mater.* **2007**, *6*, 652–655.
15. Dan, Y. P.; Lu, Y.; Kybert, N. J.; Luo, Z.; Johnson, A. T. C. Intrinsic Response of Graphene Vapor Sensors. *Nano Lett.* **2009**, *9*, 1472–1475.
16. Fan, S.; Srivastava, A.; Dravid, V. P. Nanopatterned Polycrystalline ZnO for Room Temperature Gas Sensing. *Sens. Actuators, B* **2010**, *144*, 159–163.
17. Korotcenkov, G. Metal Oxides for Solid-State Gas Sensors: What Determines Our Choice?. *Mater. Sci. Eng., B* **2007**, *139*, 1–23.
18. Doll, T.; Lechner, J.; Eisele, I.; Schierbaum, K.; Gopel, W. Ozone Detection in the ppb Range with Work Function Sensors Operating at Room Temperature. *Sens. Actuators, B* **1996**, *34*, 506–510.
19. Fan, S.; Srivastava, A.; Dravid, V. P. UV-Activated Room-Temperature Gas Sensing Mechanism of Polycrystalline ZnO. *Appl. Phys. Lett.* **2009**, *95*, 142106.
20. Peng, N.; Zhang, Q.; Lee, Y.; Tan, O.; Marzari, N. Gate Modulation in Carbon Nanotube Field Effect Transistors-Based NH_3 Gas Sensors. *Sens. Actuators, B* **2008**, *132*, 191–195.

21. Radisavljevic, B.; Radenovic, A.; Brivio1, J.; Giacometti, V.; Kis, A. Single-Layer MoS_2 Transistors. *Nat. Nanotechnol.* **2011**, *6*, 147–150.
22. Wang, H.; Yu, L.; Lee, Y.; Shi, Y.; Hsu, A.; Chin, M. L.; Li, L.; Dubey, M.; Kong, J.; Palacios, T. Integrated Circuits Based on Bilayer MoS_2 Transistors. *Nano Lett.* **2012**, *12*, 4674–4680.
23. Jariwala, D.; Sangwan, V. K.; Late, D. J; Johns, J. E.; Dravid, V. P.; Marks, T. J.; Lauhon, L. J.; Hersam, M. C. Band-like Transport in High Mobility Unencapsulated Single-Layer MoS_2 Transistors. *Appl. Phys. Lett.* **2013**, *102*, 173107.
24. Kim, S.; Konar, A.; Hwang, W.; Lee, J. H.; Lee, J.; Yang, J.; Jung, C.; Kim, H.; Yoo, J.; Choi, J.; *et al.* High-Mobility and Low-Power Thin-Film Transistors Based on Multilayer MoS_2 Crystals. *Nat. Commun.* **2012**, *3*, 1011.
25. Matte, H. S. S. R.; Gomathi, A.; Manna, A. K.; Late, D. J.; Datta, R.; Pati, S. K.; Rao, C. N. R. MoS_2 and WS_2 Analogues of Graphene. *Angew. Chem., Int. Ed.* **2010**, *49*, 4059–4062.
26. Late, D. J.; Liu, B.; Matte, H. S. S. R.; Rao, C. N. R.; Dravid, V. P. Rapid Characterization of Ultrathin Layers of Chalcogenides on SiO_2/Si Substrates. *Adv. Funct. Mater.* **2012**, *22*, 1894–1906.
27. Yin, Z.; Li, H.; Li, H.; Jiang, L.; Shi, Y.; Sun, Y.; Lu, G.; Zhang, Q.; Chen, X.; Zhang, H. Single-Layer MoS_2 Phototransistors. *ACS Nano* **2012**, *6*, 74–80.
28. Ayari, A.; Cobas, E.; Ogundadegbe, O.; Fuhrer, M. S. Realization and Electrical Characterization of Ultrathin Crystals of Layered Transition-Metal Dichalcogenides. *J. Appl. Phys.* **2007**, *101*, 014507.
29. Ghatak, S.; Pal, A. N.; Ghosh, A. Nature of Electronic States in Atomically Thin MoS_2 Field-Effect Transistors. *ACS Nano* **2011**, *5*, 7707–7712.
30. Late, D. J.; Liu, B.; Matte, H. S. S. R.; Dravid, V. P.; Rao, C. N. R. Hysteresis in Single-Layer MoS_2 Field Effect Transistors. *ACS Nano* **2012**, *6*, 5635–5641.
31. Qiu, H.; Pan, L.; Yao, Z.; Li, J.; Shi, Y.; Wang, X. Electrical Characterization of Back-Gated Bi-layer MoS_2 Field-Effect Transistors and the Effect of Ambient on Their Performances. *Appl. Phys. Lett.* **2012**, *100*, 123104.
32. Castellanos-Gomez, A.; Agraït, N.; Rubio-Bollinger, G. Optical Identification of Atomically Thin Dichalcogenide Crystals. *Appl. Phys. Lett.* **2010**, *96*, 213116.
33. Kashid, R. V.; Late, D. J.; Chou, S. S.; Huang, Y.; De, M.; Joag, D. S.; More, M. A.; Dravid, V. P. Enhanced Field-Emission Behavior of Layered MoS_2 Sheets. *Small* **2013**, 10.1002/smll.201300002.
34. Late, D. J.; Liu, B.; Luo, J.; Yan, A.; Matte, H. S. S. R.; Grayson, M.; Rao, C. N. R.; Dravid, V. P. GaS and GaSe Ultrathin Layer Transistors. *Adv. Mater.* **2012**, *24*, 3549–3554.
35. Nag, A.; Raidongia, K.; Datta, R.; Hembaram, K. P. S. S.; Waghmare, U. V.; Rao, C. N. R. Graphene Analogues of BN: Novel Synthesis and Properties. *ACS Nano* **2010**, *4*, 1539–1544.
36. Gorbachev, R. V.; Riaz, I.; Nair, R. R.; Jalil, R.; Britnell, L.; Belle, B. D.; Hill, E. W.; Novoselov, K. S.; Watanabe, K.; Taniguchi, T.; *et al.* Hunting for Monolayer Boron Nitride: Optical and Raman Signatures. *Small* **2011**, *7*, 465–468.
37. Dean, C. R.; Young, A. F.; Meric, I.; Lee, C.; Wang, L.; Sorgenfreil, S.; Watanabe, K.; Taniguchi, T.; Kim, P.; Shepard, K. L.; *et al.* Boron Nitride Substrates for High-Quality Graphene Electronics. *Nat. Nanotechnol.* **2011**, *5*, 722–726.
38. Zeng, H.; Zhi, C.; Zhang, Z.; Wei, X.; Wang, X.; Guo, W.; Bando, Y.; Golberg, D. "White Graphenes": Boron Nitride Nanoribbons *via* Boron Nitride Nanotube Unwrapping. *Nano Lett.* **2010**, *10*, 5049–5055.
39. Song, L.; Ci, L.; Lu, H.; Sorokin, P. B.; Jin, C.; Ni, J.; Kvashnin, A. G.; Kvashnin, D. G.; Lou, J.; Yakobson, B. I.; *et al.* Large Scale Growth and Characterization of Atomic Hexagonal Boron Nitride Layers. *Nano Lett.* **2010**, *10*, 3209–3215.
40. Lee, C.; Li, Q.; Kalb, W.; Liu, X.; Berger, H.; Carpick, R. W.; Hone, J. Frictional Characteristics of Atomically-Thin Sheets. *Science* **2010**, *328*, 76–80.
41. Staley, N. E.; Wu, J.; Eklund, P.; Liu, Y.; Li, L.; Xu, Z. Electric Field Effect on Superconductivity in Atomically Thin Flakes of $NbSe_2$. *Phys. Rev. B* **2009**, *80*, 184505.
42. Frindt, R. F. Superconductivity in Ultrathin $NbSe_2$ Layers. *Phys. Rev. Lett.* **1972**, *28*, 299–301.
43. Fang, H.; Chuang, S.; Chang, T. C.; Takei, K.; Takahashi, T.; Javey, A. High-Performance Single Layered WSe_2 p-FETs with Chemically Doped Contacts. *Nano Lett.* **2012**, *12*, 3788–3792.
44. Liu, W.; Kang, J.; Sarkar, D.; Khatami, Y.; Jena, D.; Banerjee, K. Role of Metal Contacts in Designing High-Performance Monolayer n-Type WSe_2 Field Effect Transistors. *Nano Lett.* **2013**, *13*, 1983–1990.
45. Splendiani, A.; Sun, L.; Zhang, Y.; Li, T.; Kim, J.; Chim, C. Y.; Galli, G.; Wang, F. Emerging Photoluminescence in Monolayer MoS_2. *Nano Lett.* **2010**, *10*, 1271–1275.
46. Eda, G.; Yamaguchi, H.; Voiry, D.; Fujita, T.; Chen, M.; Chhowalla, M. Photoluminescence from Chemically Exfoliated MoS_2. *Nano Lett.* **2011**, *11*, 5111–5116.
47. Li, H.; Yin, Z.; He, Q.; Li, H.; Huang, X.; Lu, G.; Fam, D. W. H.; Tok, A. L. Y.; Zhang, Q.; Zhang, H. Fabrication of Single- and Multilayer MoS_2 Film-Based Field-Effect Transistors for Sensing NO at Room Temperature. *Small* **2012**, *8*, 63–67.
48. He, Q.; Zeng, Z.; Yin, Z.; Li, H.; Wu, S.; Huang, X.; Zhang, H. Fabrication of Flexible MoS_2 Thin-Film Transistor Arrays for Practical Gas-Sensing Applications. *Small* **2012**, *8*, 2994–2999.
49. Perkins, F. K.; Friedman, A. L.; Cobas, E.; Campbell, P. M.; Jernigan, G. G.; Jonker, B. T. Chemical Vapor Sensing with Monolayer MoS_2. *Nano Lett.* **2013**, *13*, 668–673.
50. Lee, C.; Yan, H.; Brus, L. E.; Heinz, T. F.; Hone, J.; Ryu, S. Anomalous Lattice Vibrations of Single- and Few-Layer MoS_2. *ACS Nano* **2010**, *4*, 2695–2700.
51. Dey, S.; Matte, H. S. S. R.; Shirodkar, S. N.; Waghmare, U. V.; Rao, C. N. R. Charge-Transfer Interaction between Few-Layer MoS_2 and Tetrathiafulvalene. *Chem.—Asian J.* **2013**, 10.1002/asia.201300174.
52. Shi, Y.; Huang, J.; Jin, L.; Hsu, Y.; Yu, S. F.; Li, L.; Yang, H. Y. Selective Decoration of Au Nanoparticles on Monolayer MoS_2 Single Crystals. *Sci. Rep.* **2013**, *3*, 1839.
53. Najmaei, S.; Liu, Z.; Ajayan, P. M.; Lou, J. Thermal Effects on the Characteristic Raman Spectrum of Molybdenum Disulfide (MoS_2) of Varying Thicknesses. *Appl. Phys. Lett.* **2012**, *100*, 013106.
54. Thurston, T. R.; Wilcoxon, J. P. Photooxidation of Organic Chemicals Catalyzed by Nanoscale MoS_2. *J. Phys. Chem. B* **1999**, *103*, 11–17.
55. Kolmakov, A.; Klenov, D. O.; Lilach, Y.; Stemmer, S.; Moskovits, M. Enhanced Gas Sensing by Individual SnO_2 Nanowires and Nanobelts Functionalized with Pd Catalyst Particles. *Nano Lett.* **2005**, *5*, 667–673.
56. Buscema, M.; Barkelid, M.; Zwiller, V.; van der Zant, H. S. J.; Steele, G. A.; Castellanos-Gomez, A. Large and Tunable Photothermoelectric Effect in Single-Layer MoS_2. *Nano Lett.* **2013**, *13*, 358–363.
57. Chen, G.; Paronyan, T. M.; Pigos, E. M.; Harutyunyan, A. R. Enhanced Gas Sensing in Pristine Carbon Nanotubes under Continuous Ultraviolet Light Illumination. *Sci. Rep.* **2012**, *2*, 343.
58. Costello, B. P. J.; Ewen, R. J.; Ratcliffe, N. M.; Richards, M. Highly Sensitive Room Temperature Sensors Based on the UV-LED Activation of Zinc Oxide Nanoparticles. *Sens. Actuators, B* **2008**, *134*, 945–952.
59. Boker, T.; Severin, R.; Muller, A.; Janowitz, C.; Manzke, R.; Vob, D.; Krüger, P.; Mazur, A.; Pollmann, J. Band Structure of MoS_2, $MoSe_2$, and α-$MoTe_2$: Angle-Resolved Photoelectron Spectroscopy and *Ab Initio* Calculations. *Phys. Rev. B* **2001**, *64*, 235305.
60. Perdew, J. P.; Burke, K.; Ernzerhof, M. Generalized Gradient Approximation Made Simple. *Phys. Rev. Lett.* **1996**, *77*, 3865.
61. Giannozzi, P.; Baroni, S.; Bonini, N.; Calandra, M.; Car, R.; Cavazzoni, C.; Ceresoli, D.; Chiarotti, G. L.; Cococcioni, M.; Dabo, I.; *et al.* Quantum Espresso: A Modular and Open-Source Software Project for Quantum Simulations of Materials. *J. Phys.: Condens. Matter* **2009**, *21*, 395502.

62. Vanderbilt, D. Soft Self-Consistent Pseudopotentials in a Generalized Eigen Value Formalism. *Phys. Rev. B* **1990**, *41*, 7892.
63. Grimme, S. Semiempirical GGA-Type Density Functional Constructed with a Long-Range Dispersion Correction. *J. Comput. Chem.* **2006**, *27*, 1787–1799.